Spatially guided nonlocal mean approach for denoising of PET images

Hossein Arabi
Division of Nuclear Medicine and Molecular Imaging, Department of Medical Imaging, Geneva University Hospital, CH-1211, Geneva 4, Switzerland

Habib Zaidi[a)]
Division of Nuclear Medicine and Molecular Imaging, Department of Medical Imaging, Geneva University Hospital, CH-1211, Geneva 4, Switzerland
Geneva University Neurocenter, Geneva University, CH-1205, Geneva, Switzerland
Department of Nuclear Medicine and Molecular Imaging, University of Groningen, University Medical Center Groningen, 9700 RB, Groningen, Netherlands
Department of Nuclear Medicine, University of Southern Denmark, DK-500, Odense, Denmark

(Received 1 October 2019; revised 13 December 2019; accepted for publication 10 January 2020; published 10 February 2020)

Purpose: Nonlocal mean (NLM) filtering proved to be an effective tool for noise reduction in natural and medical imaging. The technique relies on existing redundant information in the input image to discriminate the genuine signal from noise. However, due to the prohibitively long computation time, the search for finding similar information is confined by a predefined search window, which may hamper the performance of this filter. In this work, a spatially guided non local mean (SG-NLM) approach was proposed to overcome this issue. The proposed method was evaluated on whole-body positron emission tomography images presenting with high noise levels, which adversely affect lesion detectability and quantitative accuracy.
Methods: In the SG-NLM method, as opposed to the conventional NLM method, where a predefined search window is defined to confine exhaustive search for finding similar patterns, the information about similar patterns is extracted from the clustered version (created based on signal intensity levels) of the input image as well as information about prominent edges. The performance of the SG-NLM was evaluated against post-reconstruction NLM, Gaussian, bilateral and BayesShrink Wavelet denoising approaches. A digital phantom containing three small inserts mimicking lesions in the lung, experimental study using the Jaszczak phantom and whole-body PET/CT clinical studies were utilized to assess the performance of abovementioned denoising approaches.
Results: The SG-NLM method led to a signal-to-noise (SNR) increase from 21.3 (unfiltered PET image) to 30.1 in computer simulations of small lesions while the NLM mean filer resulted in an SNR of 29.4 ($P < 0.05$). The experimental Jaszczak phantom study demonstrated that the contrast-to-noise ratio (CNR) increased from 11.3 when using the Gaussian filter to 18.6 and 19.5 when using NLM and SG-NLM filters ($P < 0.05$), respectively. The superior performance of the SG-NLM approach was confirmed by clinical studies where the bias in malignant lesions decreased to $-2.3 \pm 1.1\%$ compared to -11.7 ± 2.4 and -2.9 ± 1.1 achieved using the Gaussian and NLM methods ($P < 0.05$), respectively.
Conclusions: The proposed SG-NLM achieves promising compromise between noise reduction and signal preservation compared to the conventional NLM method. The superior performance of the SG-NLM method was accomplished without adding extra burden to the computational complexity of the conventional NLM filter, which makes it attractive for denoising PET images. © *2020 American Association of Physicists in Medicine* [https://doi.org/10.1002/mp.14024]

Key words: curvelet transform, filtering, image quality, nonlocal means, PET

1. INTRODUCTION

Positron emission tomography (PET) provides valuable information pertinent to clinical diagnosis of a number of malignant diseases as well as staging and monitoring response to treatment. However, the clinical value of PET is hampered by the relatively low spatial resolution and high noise levels. These factors potentially skew the task of lesion detectability as well as quantitative assessment image-derived PET metrics.[1] Statistical PET reconstruction approaches, such as maximum likelihood-expectation maximization (MLEM), enable modeling of the underlying physical degradation factors to partially compensate for resolution loss and poor photon detection statistics. Nevertheless, these approaches suffer from slow convergence and noise amplification at higher number of iterations as image reconstruction is an inherently ill-posed problem.[2]

A common strategy used to reduce noise level in PET images is to employ post-reconstruction smoothing filters to enhance the ratio of the PET signal to the unwanted interference, referred to as signal-to-noise ratio (SNR).[3,4] Noise reduction, performed either post-reconstruction or embedded

within the reconstruction process, tends to encourage homogeneity of intensities within a neighborhood intended to suppress unwanted noise-induced intensity fluctuations.[5,6] To discriminate unwanted noise-induced intensity variation from meaningful signals, such as organ or lesion boundaries, edge-preserving smoothing approaches were proposed to enhance the SNR while causing minimum bias in quantification of tracer uptake. Edge-preserving filters can be implemented in the transform domain, for example, wavelet- and curvelet-based filters,[7,8] in spatial domain, for example, bilateral filter,[9,10] or using hybrid dual-domain approaches.[11,12] These approaches enable reducing noise while preserving the prominent signal from meaningful structures by penalizing the smoothing power considering the gradient of edges. Complementary information that can be derived from anatomical images on hybrid imaging systems, such as PET/computed tomography (CT) and PET/magnetic resonance imaging (MRI), can potentially assist edge-preserving denoising approaches to distinguish genuine edges from factitious noise-induced fluctuations. However, the PET signals reflecting the underlying biological function of tissues, do not always coincide with the anatomical boundaries that can be extracted from CT or MR images, which might mislead edge-preserving approaches.[13,14]

Most edge-preserving techniques, such as bilateral filtering, rely only on neighboring voxels and are thus unable to catch nonlocal similarities existing throughout the image. As PET images suffer from low spatial resolution, these methods consider only the local information as the cause of blurring and structure loss due to the deficiency of information within a small neighborhood. In this regard, the nonlocal mean (NLM) method[15] proved to be efficient for noise reduction of low SNR images with the capability of preserving underlying structures by exploring nonlocal areas to extract similar information.[14]

The NLM method has been utilized for noise reduction in PET images with some modifications to enhance its overall performance or to adapt it for specific applications owing to its superior performance in preserving the underlying structures. In dynamic PET imaging where short acquisition time results in high noise levels, NLM was employed for noise reduction with modifications to account for temporal neighbor patches from different time frames.[16] The NLM denoising technique was also used within the PET image reconstruction process (in the form of patch-based denoising) to avoid noise propagation.[17] Similarity measurement between patches of voxels in PET images, when the NLM method is applied, can be extended to include anatomical images to increase the robustness and accuracy of the measurements.[14]

In principle, the NLM method explores nonlocal areas to find/extract redundant information, such as repeated patterns or prolonged edges, thereby enabling effective noise and signal discrimination. Ideally, the NLM method should scrutinize the entire image searching for similar patches of voxels; however, this approach would be prohibitively computationally expensive. This issue is particularly severe when the NLM is applied on three-dimensional (3D) images. To address this issue, a search window in the vicinity of the target voxel is defined to confine the process of redundant information extraction to a small subimage area. This approach may hamper the performance of the NLM method as a similar pattern and information residing outside the search window cannot be exploited for effective noise removal.[18,19]

The objective of this work was to propose a solution to this hurdle to enable efficient implementation of the NLM algorithm, particularly in 3D PET imaging. The proposed approach exploits a clustered version of the original image (based on different intensity levels and prominent edges) to guide the NLM method in finding similar patterns without adding to the overall computational burden of the method.[20] A similar idea has been applied in the quest of a joint solution for segmentation, smoothing and partial volume correction of PET images where the information extracted from segmented PET images is propagated through denoising and partial volume reduction.[19] In this work, we focus on the denoising of whole-body PET images by modification of the NLM method to make it particularly sensitive to meaningful small structures and edges using information residing in the clustered image. Moreover, an automated noise variance estimator was employed for efficient parameter setting in the NLM method based on the noise in the input image to establish an optimal compromise between noise removal and signal preservation.

The proposed approach was evaluated against the conventional NLM method using computer simulations, experimental phantom and clinical whole-body PET/CT studies. Moreover, the bilateral and Gaussian filters (in spatial domain) and BayesShrink wavelet method (in the transform domain) were included in the evaluation for the sake of completeness.

2. MATERIALS AND METHODS

For effective denoising, the free parameters governing the degree of noise removal should be adjusted according to the actual noise level present in PET images. A rough estimate of noise level in PET images would confine the choice of free parameters setting for each of the abovementioned filters. To this end, a novel noise estimator from a single image based on Bayesian maximum a posteriori probability (MAP) inference was used in order to infer the noise level function from PET images.[21] Once the noise level in PET images is estimated, free parameters of the filters are adjusted accordingly to enhance the quality of noise reduction as well as signal preservation. In the following, we elaborate on the algorithm used for noise variance estimation and the different denoising approaches evaluated in this work.

2.A. Noise variance estimation

In this work, we exploited the method developed in Ref. [21] to estimate the upper bound of the noise level from noisy PET images independently without any prior knowledge

about the noise content. This model is based on generating a piecewise smooth version of the original noisy image, thereby the noise level correlation with respect to the signal intensity is established through a Bayesian MAP framework to estimate the noise variance.

The noise level estimation would be fairly straightforward provided the intensity of the underlying noise-free image is constant. Even though this is very unlikely in practice, a similar concept can be realized by dividing the input noisy image into piecewise smooth regions. Image voxels are grouped into different regions according to intensity similarity and spatial connectivity using a K-means clustering method.[22] Image clustering was modified to generate patches of voxels having similar size where each one is represented by a mean intensity and variance to form for all segments. The estimation of noise variance can be simply performed by fitting a function to all sample points of variance. However, since the estimates of variance samples for each segment are noisy, the factitious outlier samples could bias the estimation of the noise function. Therefore, a probabilistic inference framework was developed to involve all sample points while constraining the variance estimate to be less vulnerable to the outliers. A detailed description of the algorithm and optimization process is presented in the Supplemental Material and in Ref. [21].

2.B. Nonlocal mean (NLM) filter

The nonlocal mean filter relies on the fact that natural images usually contain redundant information in the form of similar or repeated patterns, elongated edges, and symmetrical structures. The NLM filter takes advantage of the existing redundant information for noise suppression through finding similar patches of the image representing similar patterns or intensity distributions. By taking the average of the selected patches, the underlying pattern would be preserved while uncorrelated noise component will be reduced. Conventionally, for each voxel, the averaging process is weighted based on similarity between the patches of the image centered at the target voxel and a number of selected similar patches. The search for finding similar patches plays a determining role in the performance of the NLM filters, which is normally conducted within a predefined spatial constraint referred to as search window. This search window is normally defined as a fixed subdimension of the image to limit the search space where an exhaustive search throughout the image could be computationally demanding. However, to enhance the performance of the NLM filter, the whole image was explored at the cost of higher computation burden.[15] The mathematical formulation of the conventional NLM method is provided in Supplemental Material.

2.C. Spatially guided NLM (SG-NLM) filter

The SG-NLM approach shares the same core of the conventional NLM filter formulated in eq. (4) of the Supplemental Material. The major modification performed is through the selection of $v(p_j)$ patches to be contrasted with the target patch $v(p_i)$ and defining the similarity weights $w(i,j)$. In the conventional NLM approach, a fixed-size window centered at p_i (called search window) is defined to confine the exhaustive search to find the similar patches $v(p_j)$. The major limitation associated with this approach is that the window is confined to the vicinity of the target voxel (p_i) with limited predefined size. For the sake of computation time, the search window cannot be large enough to cover the weighty part of the image (Fig. 1 upper panel). Hence, many similar patches located outside of the search window would be overlooked, thereby impacting the quality of image filtering. This issue would be much more profound in 3D images (for instance PET images) where many similar patches may reside in far slices.

In the SG-NLM approach, the search window is replaced with a smart approach to detect and select similar patches. Firstly, PET images are converted to a piecewise smooth version where voxels with similar intensity values (within a variability threshold) are assigned similar labels. This "clustered" image is generated using the K-means clustering algorithm, also employed for noise variance estimation in the previous Section 2.A. This method takes continuously valued PET images (in SUV unit) as input to generate clustered images according to a certain number of intensity levels. In this work, six intensity levels (including background air) resulted in superior performance compared to other intensity levels considering the SNR and bias in the filtered images. An example of a clustered image generated from the PET image in Fig. 1(c) is shown in Fig. 1(d). It should be noted that the K-means clustering algorithm takes the local connectivity (among the voxels) into account, yet the voxels belonging to a common cluster (or label) are not necessarily connected throughout the 3D image. Hence, the labels in the clustered image represent the SUV level in the original PET image and also the piece-wise intensity variation across the voxels. Moreover, to emphasize on prominent edges, an additional label was added to the clustered image which stands for significant and sharp edges (corresponding to e.g. organ/lesion boundaries) as illustrated separately in Fig. 1(e). To this end, the Sobel edge detection approach[23] was employed to generate a binary map of the prominent edges in the PET image. The edge map is displayed separately for the sake of better visualization in Fig. 1(e).

To filter a voxel in the original PET image [Fig. 1(c)] given the clustered image, the cluster label that the target voxel (or target patch) belongs to is determined. Subsequently, rather than running an exhaustive search within the search window to find patches similar to the target patch (as is performed in conventional NLM), the patch search is solely performed within the area with the same cluster label. The rationale behind this strategy is that patches (or voxels) belonging to the same cluster number are very likely to share the same structures/patterns, which enhances the effectiveness of the denoising process through exploiting correlated information (and non-correlated noise behavior) in the image patches. In other words, finding similar patches in other areas with different cluster numbers is very unlikely, if not impossible, due

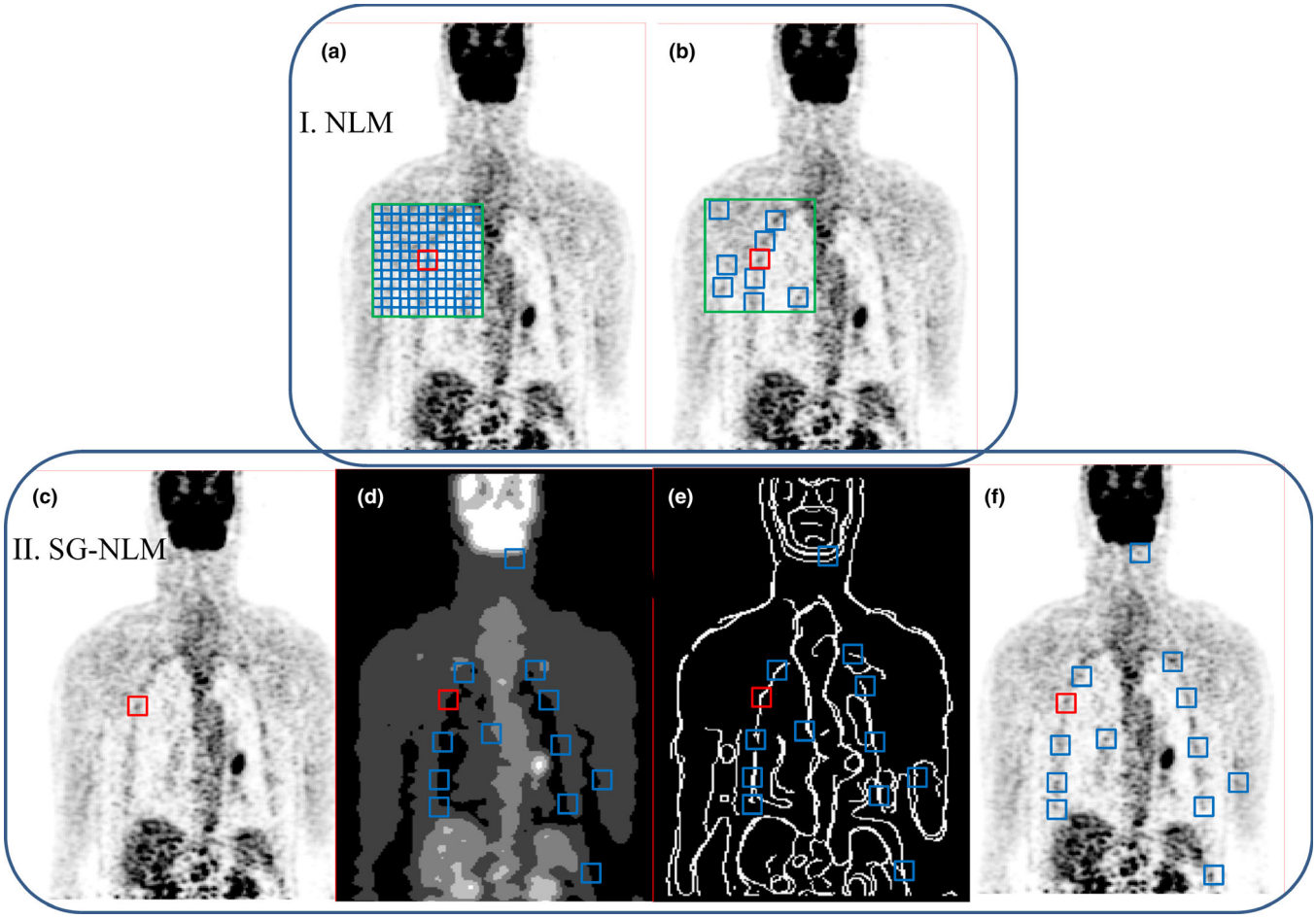

FIG. 1. The procedure of finding similar patches in the conventional nonlocal mean and spatially guided NLM filters. (a) Search window and the entire corresponding patches to be examined for similarity. (b) Similar patches in the search window. (c) Target voxel in the original positron emission tomography (PET) image. (d) Clustered image, (e) Edge map and (f) Original PET image with similar patches. [Color figure can be viewed at wileyonlinelibrary.com]

to the large intensity or structural differences. As such, these areas are excluded from the search process to find similar patches. Moreover, this allows exploring the whole 3D image. For, instance, if the target voxel resides on a prominent edge, such as the example in Figs. 1(c) to 1(f), the search for finding similar patches resembling the target patch (red box in Fig. 1) is only conducted on the edge map throughout the 3D image.

The search to find similar patches in the SG-NLM algorithm is performed as follows. First, given the clustered image, the voxels belonging to the same cluster number are stored in an array in a chronological order according to their location in the PET image. Subsequently, for the target voxel (or patch to be filtered), the cluster number is determined and based on which N (here 200) patches are randomly selected from the array corresponding to the same cluster number. It should be emphasized that the priority is given to patches closer to the target voxel to take advantage of the information lying in the near neighborhood, such as repeated patterns or elongated edges. To this end, one-fourth of the samples are taken from patches within $3 \times 3 \times 3$ cm neighborhood of the target voxel. The randomly selected patches are inserted into supplemental eq. (4) to perform the main process of denoising. This approach allows exploring the entire 3D image to detect similar patches without adding to the computational complexity of the algorithm. In the SG-NLM approach, instead of setting the search window, the number of patches to be selected from the entire image is determined by the user. In this work, a patch number of 200 was selected for the SG-NLM filter with the intention of rendering the computational time equivalent to a search window of 16×16 voxels in the conventional NLM algorithm. Given the patches selected by this approach, the rest of the SG-NLM approach is similar to the conventional NLM approach.

2.D. BayesShrink wavelet filter

Image denoising by means of the wavelet transform attempts to identify and remove the noise present in the image based on the frequency content of the image. In principle, the image is first transformed into the wavelet domain and then nonlinear thresholding is applied on the frequency content of the image. Finally, the remaining frequency coefficients are transformed back into the spatial domain via the inverse

wavelet transform. The efficiency of the wavelet denoising approaches depends to a great extent on the choice of thresholding parameters. The noise present in PET images can be modeled as an additive function to the original noiseless signal according to Eq. (1).

$$\mathrm{Im}(x) = Y(x) + N(x) \tag{1}$$

where *Im(x)* is the observed image, which consists of the uncorrupted part *Y(x)* plus the noise function *N(x)*. The wavelet transform operator decomposes an image into diagonal, horizontal and vertical subbands. The BayesShrink method (BW) assumes a generalized Gaussian distribution for image coefficients at each subband governed by standard deviation, wherein the threshold to discriminate noise is inversely proportional to the standard deviation of the noise in the high frequency subband.[24] A detailed description of the BayesShrink method is provided in Supplemental Material.

2.E. Simulation, experimental and clinical studies

The proposed SG-NLM approach was investigated against the conventional NLM, BayesShrink wavelet as well as bilateral and conventional post-reconstruction Gaussian filters. The evaluation of the abovementioned approaches was carried out using computer simulations, experimental phantom and clinical studies.

2.E.1. Computer simulations

A 3D digital thorax phantom containing three small lesions (10 × 10 × 10 mm) was simulated in a matrix of 256 × 256 × 100 with a voxel size of 2.5 mm^3. This phantom was used to model an ^{18}F-FDG PET/CT thoracic scan (Fig. S1). Attenuation coefficients of 0.1 and 0.03 cm^{-1} were assigned to soft tissue and lung regions, respectively. Two out of the three tumors (T1 and T3) were located in the lung with tumor to background contrast ratios of 4:1 (T1) and 2:1 (T3) whereas the other tumor (T2) was located in soft tissue with a contrast ratio of 3:1. In the computer simulation study, only photon attenuation was taken into account in a 2D image reconstruction framework. To model the finite resolution of the PET scanner, a Gaussian filter with a full-width at half-maximum (FWHM) of 6 mm was applied to blur the projections of the original phantom. Noise simulation was performed by adding twenty levels of Poisson noise to the projection data. The total number of counts was adjusted to generate a noise variance ranging from 0.001 to 0.2 in the lung region. In the projection space, the total number of counts is around 1 M per slice. The Michigan image reconstruction toolbox (MIRT) implemented in Mathwork's Matlab enviroment* was employed to perform image reconstruction using the ordered subset-expectation maximization (OSEM) algorithm using four iterations and eight subsets.

*http://web.eecs.umich.edu/~fessler/code/index.html

2.E.2. Experimental study

The physical Jaszczak phantom was exploited to perform experimental phantom studies. This phantom contains six spheres with diameters of 11.89, 14.43, 17.69, 21.79, 26.82 and 33.27 mm surrounded by a cylinder with 100 mm radius and 180 mm length referred to as background medium. The six spheres and the background medium were filled with activity concentration of 18.4 kBq/ml and 3.6 kBq/ml, respectively, to render a signal to background contrast ratio of 5:1. In total, 22 MBq was inserted into the Jaszczak phantom. The scan of the phantom was performed on a Biograph mCT PET/CT (Siemens Medical Solutions USA, Knoxville, TN, USA) in one session for 30 min. The raw PET data were saved in list-mode format, thereby enabling reconstruction of the scan at different time frames, specifically 10 s, 30 s, 1 min, 3 min, 10 min, and 30 min. Hence, six datasets of the phantom were obtained containing six different noise levels. The list-mode PET data were reconstructed using OSEM algorithm with four iterations and eight subsets using the e7 tool (Siemens Healthcare, Knoxville, TN) with a matrix of 400 × 400 × 45 voxels and size 2 × 2 × 5 mm. CT-based scatter and attenuation correction were also performed.

2.E.3. Clinical studies

The clinical evaluation was carried out using 15 clinical whole-body ^{18}F-FDG PET/CT studies (mean age ± SD = 62 ± 6 yr and mean weight ± SD = 67.5 ± 8 kg) performed on a Biograph 64 True Point scanner (Siemens Healthcare, Erlangen, Germany). The patients were referred for PET/CT scans for staging of head and neck malignancies. An activity of 371 ± 23 MBq (average ± SD) was administrated prior to PET examination using 5-6 bed positions with a total acquisition time of 15–18 min (3 min per bed position). Positron emission tomography /CT scans were reconstructed using the e7 tool (Siemens Healthcare, Knoxville, TN) by means of the ordinary Poisson ordered subset-expectation maximization (OP-OSEM) iterative algorithm with default reconstruction parameters used in the clinic (four iterations and eight subsets). Gaussian post-reconstruction filtering used by default was deactivated to acquire original PET images. Positron emission tomography images were reconstructed using a matrix of 168 × 168 × 205 voxels with a voxel dimension of 4 × 4 × 2.5 mm^3.

The performance of the different denoising approaches was examined on hot spots and malignant lesions present in the 15 patient studies. To this end, 40 volumes of interests (VOIs) were drawn on hot spots and malignant lesions with no more than 4 VOIs defined on a single patient. Most of the lesions were located in the head and neck region (28 VOIs) and the rest in the liver (7 VOIs) and lungs (5 VOIs). The size of VOIs drawn on the lesions ranged from 0.4 to 1.9 ml. To measure the tumor to background contrast, the corresponding background VOIs (with the same size) were drawn on the same regions where the lesions were located.

Though the bulk of quantitative evaluation was conducted on lesion VOIs (small subset of images), 40 VOIs in total corresponding to 40 lesions (including their respective backgrounds) were assessed in this work. More importantly, these lesions were located in different body regions (lungs, liver and head and neck) with various lesion-to-background contrasts. Moreover, the lung region was segmented from CT images of 15 patients to extract the mean and standard deviation of tracer uptake within the lung region before and after applying the different denoising techniques.

2.F. Quantitative analysis

The proposed SG-NLM approach was compared to conventional NLM, BayesShrink Wavelet (BW), bilateral[9] and Gaussian post-reconstruction denoising approaches using the simulation, experimental and clinical studies. In all studies, prior to applying the denoising approaches, the noise variance estimator was employed to assess the levels of noise present in the image. Given the estimate of noise variance, the free parameters of denoising approaches were accordingly adjusted to optimize the trade-off between noise removal and signal loss.

For Gaussian filtering, a 3D kernel filter was applied in all studies, however, the kernel range varied from 2 to 10 mm FWHM for the computer simulation and experimental phantom studies depending on the existing noise levels in the images. For the clinical studies, the Gaussian kernel varied from 4 of 8 mm FWHM. The bilateral filtering, composed of two kernels in intensity and spatial domains in the form of Gaussian shapes[25] was applied slice by slice in 2D mode. Two Gaussian standard deviations, namely σ_{In} and σ_{Sp}, regulate the intensity and spatial kernels, respectively. For the spatial kernel, the standard deviation was fixed at 3.8 according to the recommendations in Ref. [9], whereas for the intensity kernel, the standard deviation (σ_{In}) was automatically adjusted according to the output of the noise variance estimator. The range of σ_{In} varied from 0.1 to 0.5 considering images normalized to one (intensity range of 0–1).

In the computer simulation and experimental phantom studies, the contrast-to-noise ratio (CNR) was measured for the tumors in the thorax phantom as well as the hot spheres in the Jaszczak phantom before (OSEM) and after applying the different denoising approaches using Eq. (2).[26]

$$CNR = \frac{\left|\mu_{target} - \mu_{background}\right|}{\sqrt{\frac{\left|\sigma^2_{target} + \sigma^2_{bakcground}\right|}{2}}} \tag{2}$$

μ_{target} and $\mu_{background}$ indicate the mean values measured in the VOIs drawn on the target and background, respectively. σ^2_{target} and $\sigma^2_{background}$ denote the corresponding standard deviations in the VOIs in the target and background, respectively. The VOIs on the targets were drawn according to the shape of the lesions or spheres and the same VOIs were placed in the background medium. Furthermore, the normalized bias and signal-to-noise ratio (SNR) were estimated for the tumors and hot spheres using Eqs. (3) and (4) (described in Ref. [14]) before and after applying the different denoising approaches.

$$Bias(\%) = \frac{100}{Nr}\sum_{i=1}^{Nr}\frac{\left|\left(\mu_{target_i} - Tv\right)\right|}{Tv} \tag{3}$$

$$SNR = \frac{\frac{1}{Nr}\sum_{i=1}^{Nr}\left(\mu_{(target)i} - \mu_{(background)i}\right)}{\frac{1}{Tb}\sum_{k=1}^{Tb}\sigma_k} \tag{4}$$

Nr indicates the number of noise realizations and Tv denotes the ground-truth intensity value within the VOIs. σ_k indicates the ensemble standard deviation measured over the entire noise realizations for each voxel (k) in the background VOI. The total number of voxels belonging to a VOI is indicated by Tb. Since the ground-truth intensity values within the VOIs are known in computer simulation and physical phantom studies, Eq. (3) was used for bias measurement. However, in the clinical studies, the bias resulting from the denoising approaches was measured against the original noisy (unfiltered) PET images using Eq. (5) owing to the absence of ground-truth uptake values.

$$Bias(\%) = \frac{\mu VOI_{denoised} - \mu VOI_{noisy}}{\mu VOI_{noisy}} \tag{5}$$

In addition, Eq. (6) was employed to calculate the SNR in clinical studies (SNR_p), where σ_i denotes the standard deviation within the background VOI and NL stands for the number of lesions/VOIs across all patients.

$$SNR_p = \frac{1}{NL}\sum_{i=1}^{NL}\frac{\left(\mu_{(target)i} - \mu_{(background)i}\right)}{\sigma_i} \tag{6}$$

In Eq. (2), the difference between the target signal and background is normalized to the standard deviation of the target and background VOIs. Conversely, the SNR for phantom and simulation studies [Eq. (4)] was calculated using the difference between the target signal and background which is normalized to the ensemble standard deviation of each voxel across noise realizations (σ_k) in the background VOI. Owing to the absence of different noise realizations in the clinical studies for each individual lesion/VOI, SNR_p [Eq. (6)] was calculated using the standard deviation computed over the background VOI.

The differences between the NLM and SG-NLM denoising approaches were investigated using the paired t-test method considering a $P < 0.05$ as statistically significant difference.

3. RESULTS

3.A. Computer simulations

Figure 2 illustrates a representative slice of the thorax phantom containing the three tumors before (OSEM) and

after applying the different denoising approaches. Residual images are also presented to give a qualitative assessment of noise reduction and signal loss achieved by each of the denoising approaches. Moreover, the profiles plotted across the three tumors are displayed in Fig. S1 demonstrating the level of signal preservation and noise smoothing. Visual inspection revealed remarkable signal loss and blurring of structures when applying the Gaussian filter. In contrast to the Gaussian filter, the BW filter led to relatively low signal loss, yet very poor noise removal. The bilateral filter exhibited an intermediate performance resulting in a balanced resolution loss and noise reduction. In this regard, the NLM and SG-NLM algorithms showed the best results achieving proper noise reduction and minimal blurring, In particular, SG-NLM resulted in lower signal loss.

The results of quantitative evaluation presented in Table I confirm the qualitative assessment. The estimation of CNR, bias and SNR for the VOIs defined on the three tumors demonstrated the overall superior performance of the proposed SG-NLM approach. As expected, the Gaussian filter led to the largest bias (up to 33.2%) in contrast to the BW and SG-NLM approaches, which achieved a bias of 25.8% and 25.9%, respectively. Despite the low signal loss (bias) achieved by the BW approach, this method led to poor SNR enhancement, from 19.5 in OSEM image to 24.4 for T3, while the Gaussian and SG-NLM filters achieved SNRs of 25.1 and 29.0, respectively. The differences between the results obtained by NLM and SG-NLM were all statistically significant except for the CNR of T1 (*P*-value of 0.07).

3.B. Experimental phantom studies

Figure 3 illustrates OSEM reconstructions of the Jaszczak phantom with acquisition times varying between 10 s and 30 min before (OSEM) and after applying the different denoising approaches. The different noise levels were realized through reconstruction of the 30 min list-mode PET data at different time points. Image reconstruction was performed for all acquisition times using the same parameters, including random, attenuation and scatter corrections. In agreement with the results of the thorax phantom, the SG-NLM approach resulted in overall less signal and resolution loss and effective

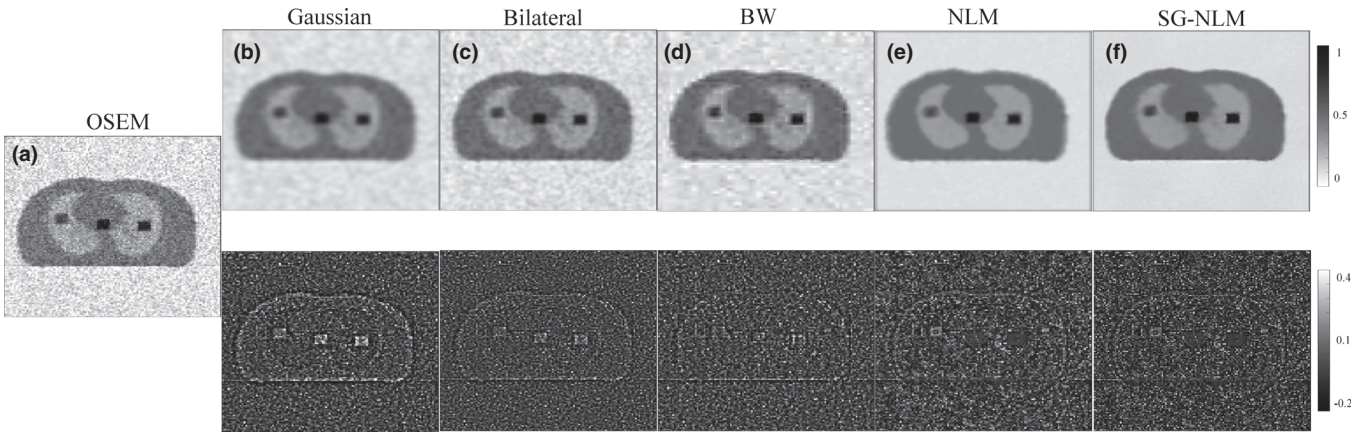

FIG. 2. Ordered subset-expectation maximization (OSEM) reconstruction of the digital thorax phantom before (a), and after noise filtering using the Gaussian (b), bilateral (c), BayesShrink method (d), nonlocal mean (E), and spatially guided NLM (F) approaches together with the corresponding residual images (OSEM — filtered image). The OSEM image displays the noise realization which led to a noise variance of 1.1.

TABLE I. Quantitative bias, contrast-to-noise ratio (CNR) and signal-to-noise ratio (SNR) estimated for the three tumors in the digital thorax phantom.

Tumor	OSEM	Gaussian	Bilateral	BW	NLM	SG-NLM	*P*-value
T1							
Bias (%)	24.3	33.2	27.6	25.8	26.8	25.9	0.03
SNR	21.4	26.9	27.4	25.8	29.1	29.9	0.04
CNR	6.4	6.8	8.6	9.2	14.4	15.1	0.07
T2							
Bias (%)	21.2	30.7	26.8	23.5	24.6	23.6	0.02
SNR	23.0	28.9	29.7	27.2	30.9	31.6	0.04
CNR	5.3	8.8	10.6	11.1	18.7	19.8	0.03
T3							
Bias (%)	16.3	25.6	22.7	19.4	20.6	19.4	0.02
SNR	19.5	25.1	26.6	24.4	28.3	29.0	0.04
CNR	7.2	13.5	16.8	17.0	25.1	26.6	0.03

BW, BayesShrink method; NLM, nonlocal mean; OSEM, ordered subset-expectation maximization; SG-NLM, spatially guided NLM.

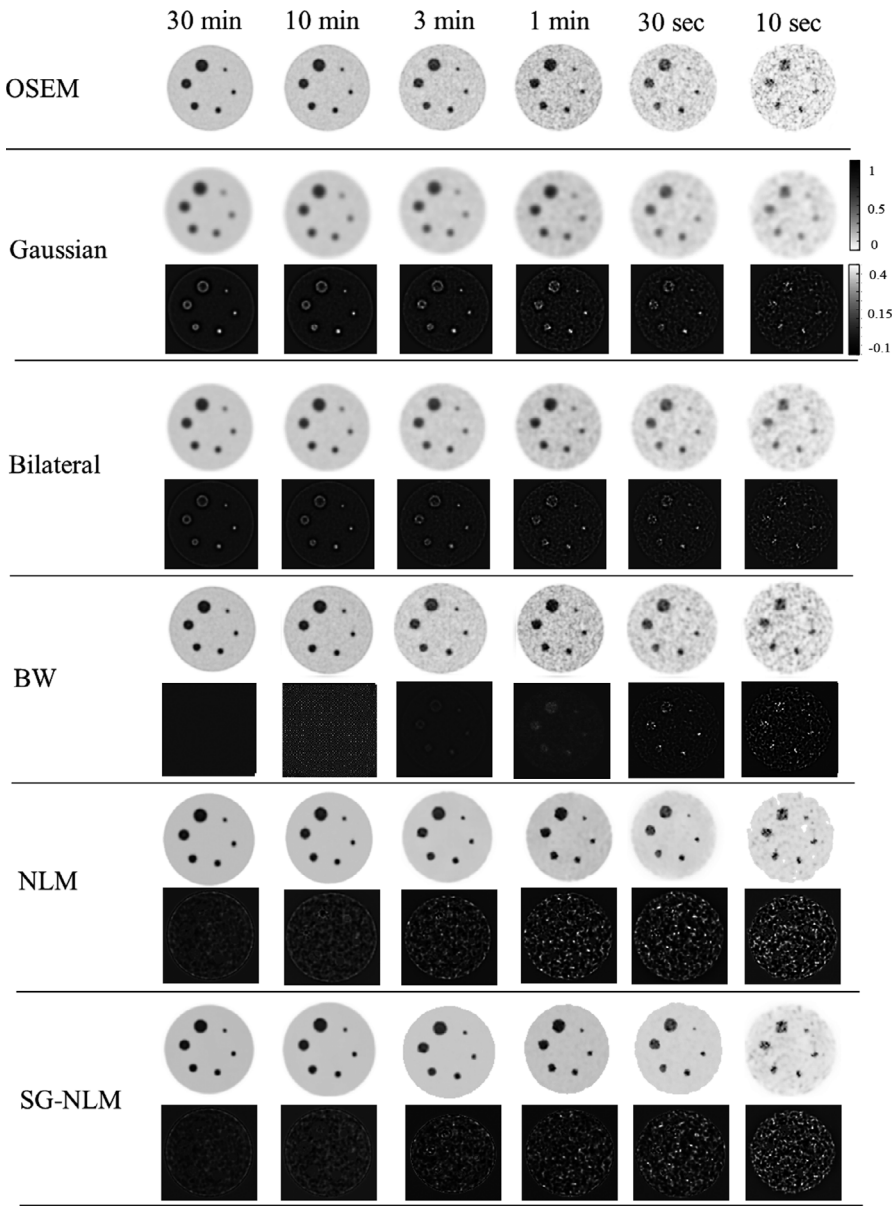

FIG. 3. The physical Jaszczack phantom reconstructed for different acquisition times before ordered subset-expectation maximization (OSEM) and after applying different the various denoising approaches together with corresponding residual images (OSEM — filtered image).

noise reduction. In this regard, BW filtering exhibited poor noise removal performance whereas Gaussian filtering led to remarkable signal loss as illustrated in the residual images.

The horizontal profiles plotted over the smallest and largest spheres of the Jaszczak phantom (Fig. 4) demonstrated considerably less resolution and signal loss when using the SG-NLM filter. This difference is more evident in the subplot for the 10 s PET image since other methods led to noticeable signal and structure loss, except the BW method at the cost of poor denoising performance. Since the mean activity concentration inside the six spheres and the background of the Jaszczak phantom were known, Eqs. (2), (3), and (4) were employed to estimate the CNR, bias and SNR for the six spheres in the Jaszczak phantom reported in Table II. The largest bias was observed in the smallest sphere (VOI 1 in Table II) when using Gaussian filtering (up to 35%) compared to 31.2% achieved by the SG-NLM approach. It should be noted that the bias was measured against the known ground-truth activity concentrations in the phantom while the OSEM image already contained 29.2% bias in the small sphere. Considering the SNR metric, SG-NLM exhibited superior performance for all VOIs followed by the conventional NLM approach. In contrast, BW and Gaussian filtering led to poor SNRs compared to the other approaches. The differences between the results obtained by NLM and SG-NLM were all statistically significant, except for the CNR of VOIs 2 and 6 (P = 0.06 and 0.08, respectively) and SNR of VOI 6 (P = 0.05).

3.C. Clinical studies

Representative sagittal views of clinical PET/CT images of a patient presenting with a lesion in the neck and non-

TABLE II. The bias, signal-to-noise ratio (SNR) and contrast-to-noise ratio (CNR) estimated for the six spheres of the Jaszczak phantom before (OSEM) and after applying the different denoising approaches. VOIs 1 to 6 correspond to the smallest to the largest spheres in the Jaszczak phantom.

VOI	OSEM	Gaussian	Bilateral	BW	NLM	SG-NLM	*P*-value
1							
Bias (%)	29.2	35.4	33.3	31.5	32.0	31.2	0.03
SNR	20.2	25.1	26.0	25.8	27.9	28.7	0.04
CNR	5.9	6.3	8.8	8.9	12.9	13.8	0.04
2							
Bias (%)	27.4	32.6	31.3	30.7	30.9	29.8	0.04
SNR	21.0	25.9	26.3	25.9	28.3	29.8	0.01
CNR	6.2	8.4	10.0	9.8	13.1	13.9	0.06
3							
Bias (%)	25.2	30.7	28.6	28.8	28.1	29.1	0.02
SNR	21.7	26.4	27.8	26.6	29.1	30.0	0.02
CNR	8.2	11.3	15.1	15.2	17.8	18.8	0.03
4							
Bias (%)	25.1	28.5	27.4	27.1	27.2	26.7	0.05
SNR	22.6	26.9	28.0	26.3	31.3	32.3	0.02
CNR	9.1	14.3	17.5	17.3	21.6	22.6	0.02
5							
Bias (%)	24.3	27.0	26.2	25.4	25.9	25.0	0.04
SNR	23.0	27.3	28.4	27.1	31.4	32.2	0.04
CNR	8.2	14.1	17.7	18.3	22.1	22.9	0.06
6							
Bias (%)	22.3	24.7	24.3	23.8	23.9	23.0	0.03
SNR	22.8	27.2	28.4	27.3	31.5	32.3	0.05
CNR	9.1	13.5	18.3	18.1	24.1	24.9	0.08

BW, BayesShrink method; NLM, nonlocal mean; OSEM, ordered subset-expectation maximization; SG-NLM, spatially guided NLM; VOI, volumes of interest.

small lung cancer are depicted in Fig. 5. Visual inspection revealed efficient noise reduction when using Gaussian, bilateral, NLM and SG-NLM approaches. In the image filtered using the BW method [Fig. 5(d)], noticeably higher noise level is seen compared to the other approaches. It should be noted that the OSEM image [Fig. 5(a)] was not processed by any post-reconstruction filter. Considering the residual images, Gaussian and bilateral filters led to noticeable loss of signal and structures compared with the residual of the BW and SG-NLM approaches.

The profile plotted on the lesions located in the neck and lung demonstrate effective noise reduction when using the SG-NLM filter while Gaussian filtering resulted in substantial contrast and signal loss (Fig. 6). The NLM filter exhibited superior performance compared to the Gaussian and bilateral approaches in terms of signal preservation and to the BW approach in terms of noise reduction. Nevertheless, the NLM approach lagged behind the SG-NLM resulting in larger loss of signal and contrast. The quantitative evaluation reported in Table III confirmed the superior performance of the SG-NLM algorithm, leading to overall bias of −2.3% compared to the original noisy image (OSEM). The NLM and BW approaches also demonstrated relatively low bias (−2.9%); however, BW led to poor SNR (27.8) compared to what is achieved by NLM (30.3) and SG-NLM (31.3) approaches, respectively. The differences between the results obtained by NLM and SG-NLM were all statistically significant, except for the lung ($P = 0.08$).

The impact of using the noise variance estimator to set the free parameters of the Gaussian, bilateral, NLM and SG-NLM smoothing approaches was investigated against using a predefined value (optimized for a broad range of noise levels) on the lung tumor (T1) in the thorax phantom. Figure 7 compares the bias (%) and SNR measured on T1 for the different filters when predefined and variable parameters were used. The deployment of the noise variance estimator improved substantially the overall performance of denoising approaches, considering the bias and SNR metrics for the entire range of noise realizations (noise variance = 0.01 − 0.2).

4. DISCUSSION

The spatially guided nonlocal mean (SG-NLM) filter was introduced in this work as a variant of the conventional NLM filter, which is easy to implement, is computationally efficient and is more effective in terms of noise reduction and signal preservation. The major modification brought to the conventional NLM is that the search window intended to limit the exhaustive search for finding similar patches is replaced with a searching scheme guided by the clustered version of the original image to conduct an efficient search for

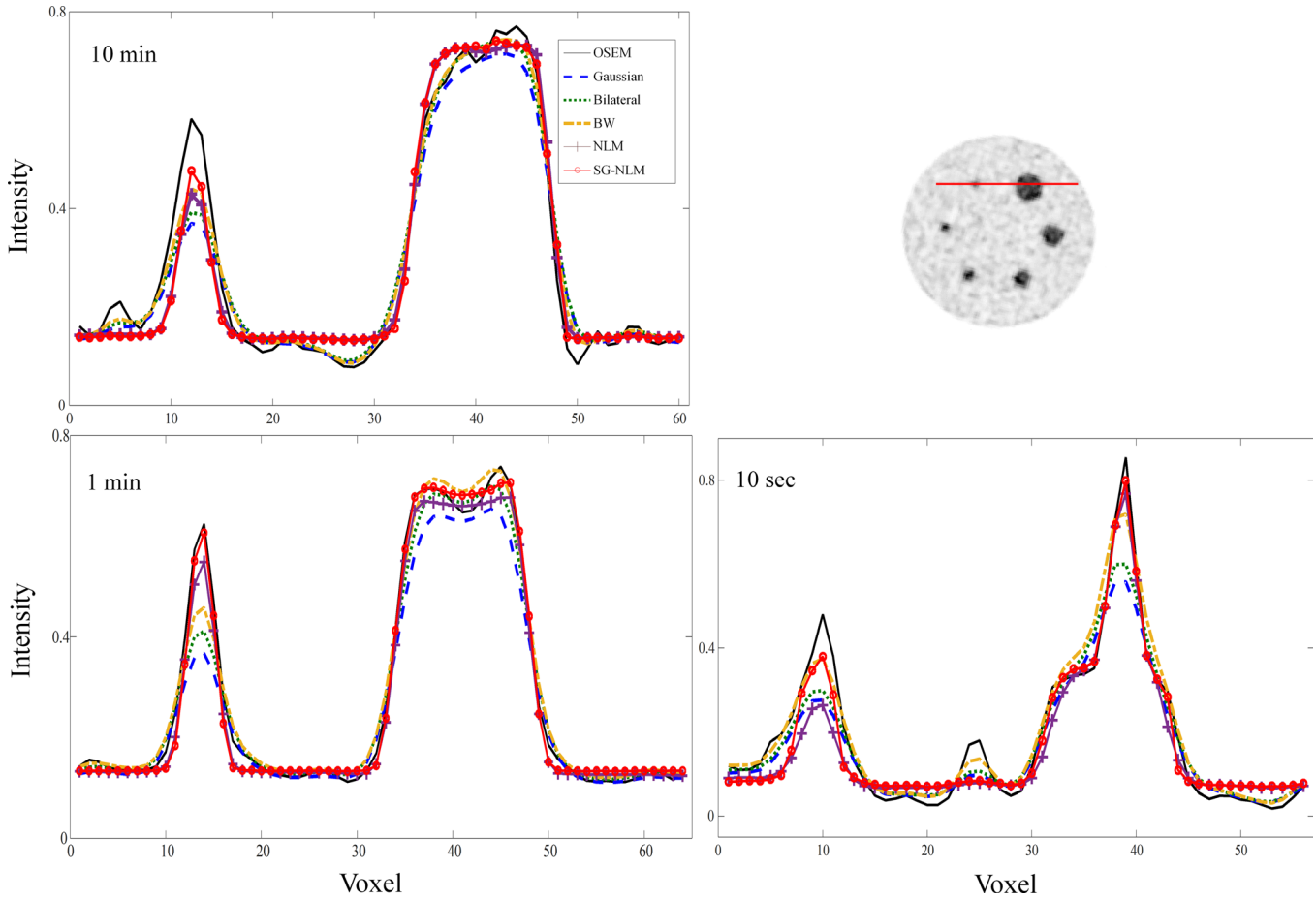

FIG. 4. Horizontal profiles drawn on the smallest (11.89 mm) and largest (33.27 mm) spheres of the Jaszczak phantom reconstructed at different acquisition times before (ordered subset-expectation maximization) and after applying the different denoising approaches. [Color figure can be viewed at wileyonlinelibrary.com]

similar patches. The proposed approach offers two major advantages: first, the information provided by the clustered image would facilitate/optimize the process of patch searching. Second, the whole image will be explored by this approach, which makes it an attractive option for 3D PET images where the repeated patterns (redundant information), such as lesions or hot nodules, might be located in slices far away from the target voxel.

The quantitative evaluation performed on the simulated digital phantom, experimental Jaszczak phantom and whole-body clinical PET/CT studies demonstrated the superior performance of the SG-NLM approach against the conventional NLM method. The SG-NLM approach led to enhanced SNR as well as reduced bias compared to the NLM method for the six spheres in the Jaszczak phantom and the lesions in the clinical studies ($p < 0.05$). The same filter core, mathematically presented in eq. (4) of the Supplemental Material, and parameters setting was employed in both SG-NLM and NLM methods (only the search strategies to find similar patches was different). Hence, the improvement brought by the SG-NLM approach results from the effective search strategy to find similar patches, where the redundant information in the whole 3D PET image was exploited.

A number of commonly used filters were evaluated in this work in an attempt to give broader and accurate view over the overall performance of the SG-NLM approach. In this regard, the bilateral and BW as well as conventional post-reconstruction Gaussian filters were included in the comparative evaluation. The conventional NLM method outperformed the other approaches resulting in less structural loss and higher SNR. This issue was mentioned to emphasize the superior performance of the NLM method compared to other methods since in 2D or very small 3D images, the performance of the NLM method would approach SG-NLM owing to the fact that the search window in the NLM could cover a significant portion of the image. As such, the information located outside the search window may be negligible for effective denoising. In the worst case scenario, the NLM and SG-NLM methods would exhibit similar performance and remain superior to the other denoising methods. It should be noted that the smoothing weights $w(i,j)$ in eq. (4) of the Supplemental Material, which indicate the level of similarities between patches of voxels, were determined from the median filtered version of the input image for both the NLM and SG-NLM methods to suppress the salt and pepper noise

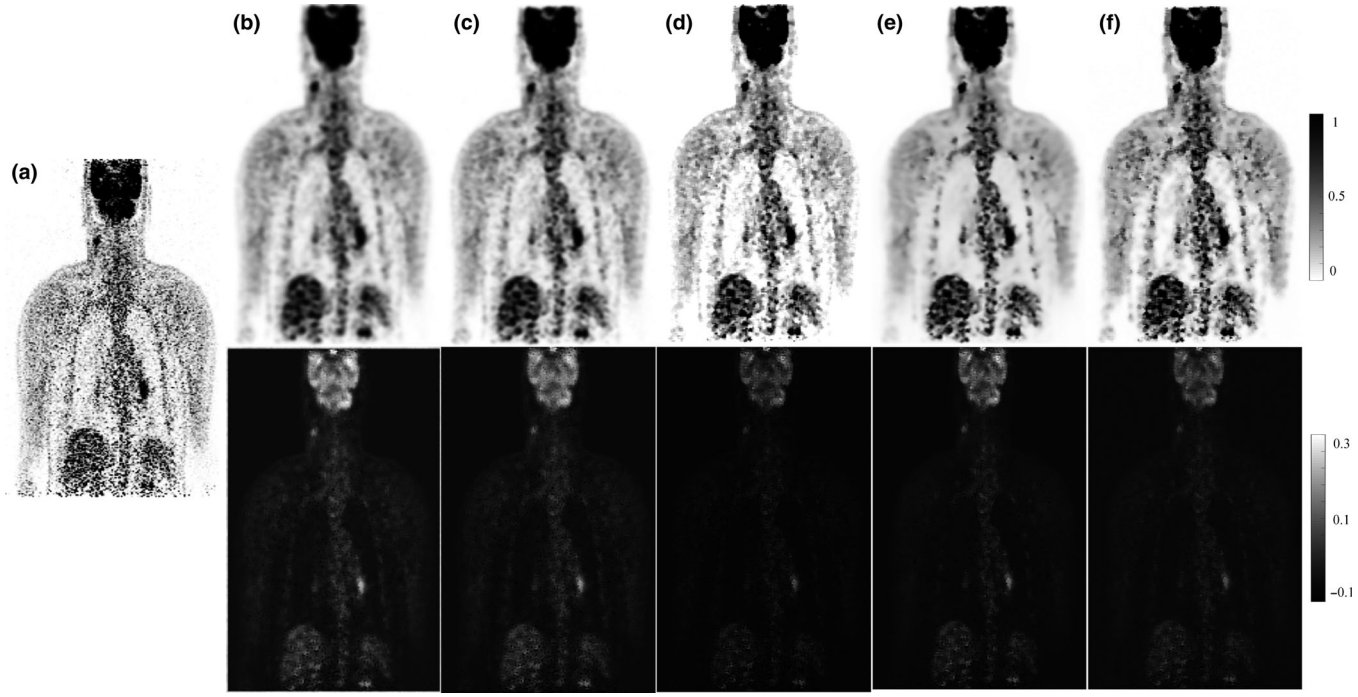

FIG. 5. Representative views of a patient positron emission tomography image with a small lesion in the neck and non-small lung cancer before (a) and after applying the following denoising approaches: Gaussian (b), bilateral (c), BayesShrink method (d), nonlocal mean (e), and spatially guided NLM (f). The corresponding residual images are also displayed.

observed in OSEM reconstructed images and enhance the robustness of the similarity measurement [14].

In principle, noise reduction methods rely on single or multiple parameters to create a balance between the degree of smoothness and preservation of the underlying structures. Most of the time, a set of predefined parameters may not lead to a desirable outcome as the parameter determination should be in accordance with the existing noise levels in the input image. To address this issue, the noise variance estimator was employed to modify the filtering parameters considering the level of noise in the input image. Figure 7 demonstrated the benefits of using variable (adaptive) parameters setting over the entire range of noise realizations. However, in static PET imaging, the noise levels would not vary dramatically from one study to another and as such, the impact of using the noise variance estimator would be limited. Nevertheless, in dynamic PET studies where the existing noise level varies noticeably from one acquisition frame to another, the adoption of variable parameter setting using the noise variance estimator would possibly result in homogenous noise removal across the different frames.

As expected, the Gaussian filter resulted in noticeable resolution and signal loss since this method is not able to discriminate genuine signal from noise-induced fluctuations. On the other hand, BW led to relatively low bias compared to Gaussian, bilateral and even conventional NLM methods, at the cost of insufficient noise suppression, leading to poor SNR in experimental phantom and clinical studies. Moreover, the bilateral filter did not show any remarkable overshooting and/or noise amplification since edge-preserving methods might amplify the noise-induced pattern in the case of strong noise signal. This phenomenon was observed in Fig. 3 for an acquisition time of 10 s where the NLM and SG-NLM approaches did not succeed to eliminate noise-driven patterns inside the largest sphere, which were reflected in the filtered images. The bilateral filter showed less sensitivity to noise-induced structures at the cost of overall lower performance in terms of SNR and bias.

The performance of SG-NLM and conventional NLM methods was compared in terms of key image quality metrics, such as SNR, CNR and bias without considering the processing time and computational burden. The number of patches in the SG-NLM method to be investigated for similarity was set at 200, which is equivalent to a search window of 16×16 voxels in the NLM method in terms of computational time. Hence, the superior performance exhibited by the SG-NLM filter was achieved without adding extra burden to the computational complexity of the conventional NLM method. Moreover, the SG-NLM filter reaches its peak performance with a patch number of less than 150, which would render this method about 20% faster than the NLM method. It should be noted that a slight increase in the search window of the NLM method, for instance from 16×16 to 22×22 voxels to explore a larger area, would increase the computational time by a factor of two.

In clinical practice, Gaussian filtering is conventionally used in the clinic (including our institution) to diminish the adverse impact of noise on qualitative interpretation of PET images. However, this approach tends to oversmooth some significant structures and skew quantitative analysis of PET images. In this regard, Gaussian filtering is considered as

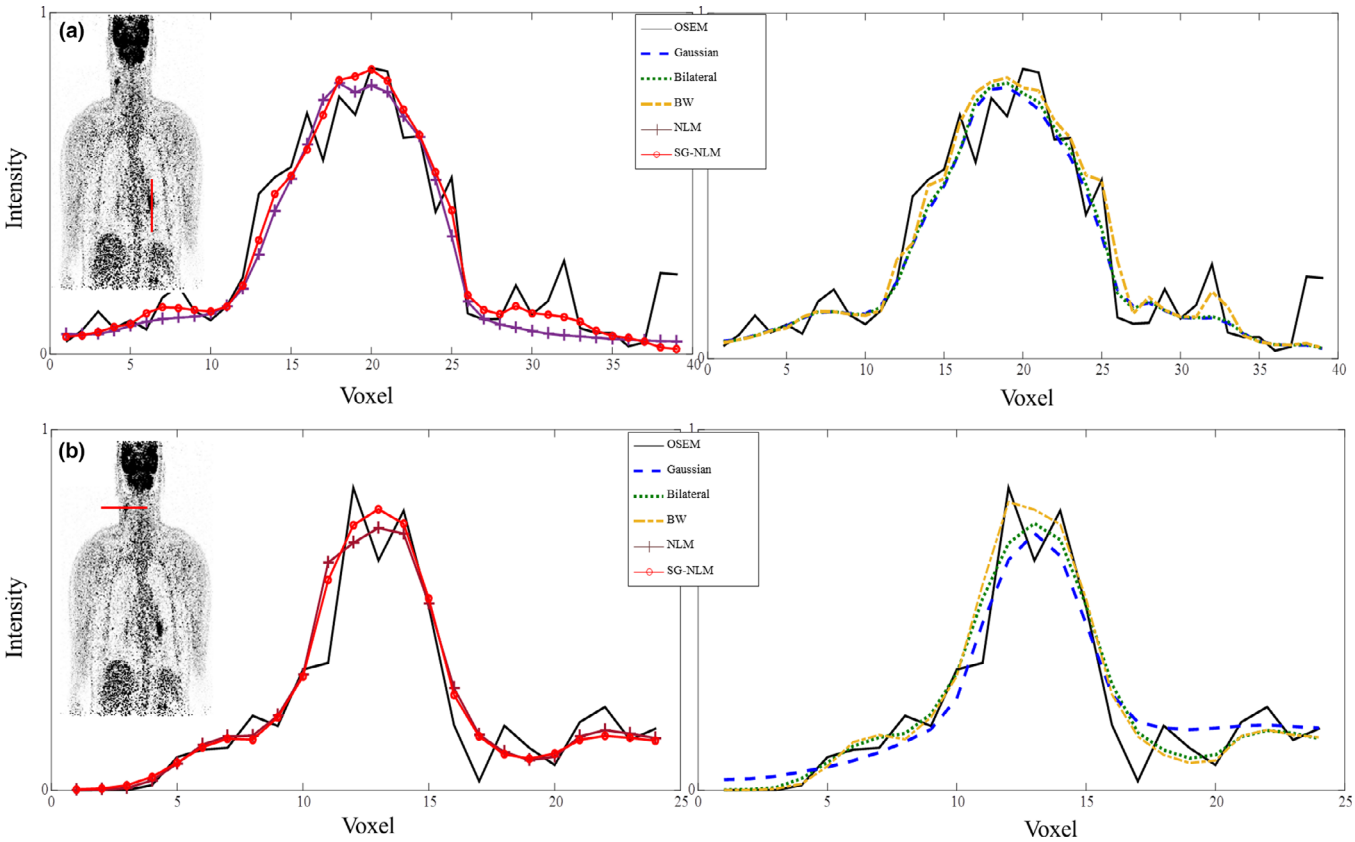

FIG. 6. The vertical profiles through the lesion located on the left lung (a) and the horizontal profiles through the lesion located in the neck (b) before (ordered subset-expectation maximization) and after applying the different denoising approaches. [Color figure can be viewed at wileyonlinelibrary.com]

TABLE III. Average SUV estimated in the lungs and lesions (standard deviation within the lung/lesion) together with the signal-to-noise ratio (SNR), contrast-to-noise ratio (CNR) and quantification bias in terms of changes (%) (±standard deviation) against the original OSEM image for the VOIs drawn on the lesions in clinical studies.

	OSEM	Gaussian	Bilateral	BW	NLM	SG-NLM	*P*-value
CNR	12.1 ± 3.6	14.2 ± 3.5	18.2 ± 3.9	17.3 ± 4.0	22.0 ± 4.1	23.1 ± 4.0	<0.01
SNR	22.4 ± 6.2	25.6 ± 5.3	28.3 ± 5.8	27.8 ± 6.1	30.3 ± 5.9	31.3 ± 5.9	0.01
Average lesion SUV (SD within the lesion)	7.4 ± 1.8 (1.4)	6.4 ± 1.7 (1.0)	6.8 ± 1.7 (0.8)	7.2 ± 1.8 (0.9)	7.0 ± 1.7 (0.6)	7.2 ± 1.7 (0.6)	0.04
Average lung SUV (SD within the lung)	0.28 ± 0.4 (0.096)	0.21 ± 0.3 (0.063)	0.21 ± 0.3 (0.057)	0.22 ± 0.3 (0.062)	0.24 ± 0.3 (0.048)	0.25 ± 0.3 (0.046)	0.08
Change (%)	—	−11.7 ± 2.4	-7.1 ± 1.8	−2.4 ± 1.9	−2.9 ± 1.1	−2.3 ± 1.1	0.03

BW, BayesShrink method; NLM, nonlocal mean; OSEM, ordered subset-expectation maximization; SG-NLM, spatially guided NLM; VOI, volumes of interest.

baseline based on which the performance of other techniques was assessed with the aim of reducing signal loss (compared to Gaussian filtering) and effectively diminishing unwanted signal fluctuations. In this regard, the proposed SG-NLM approach offers a better solution for denoising of PET images compared to conventional Gaussian filtering. However, the human visual system is capable of recognizing noise from the underlying signals and in some situations noisy PET images before denoising look more informative to human eyes (Fig. 6). Moreover, some denoising techniques may result in false lesion-like structures and/or artifacts which might render the utility of these approaches in the clinic questionable (similar cases might be visible in Fig. 6). It should be noted that this is not always the case and in certain situations, clinically significant structures reflecting the pathology might be buried under noise and could be overlooked by the human visual system. In such a situation, advanced denoising approaches (such as the SG-NLM proposed in this work with promising quantitative performance) could assist physicians to handle these cases, though they might result in some unwanted local signal alteration. A potential solution for this issue is, similar to how potential issues with CT-based

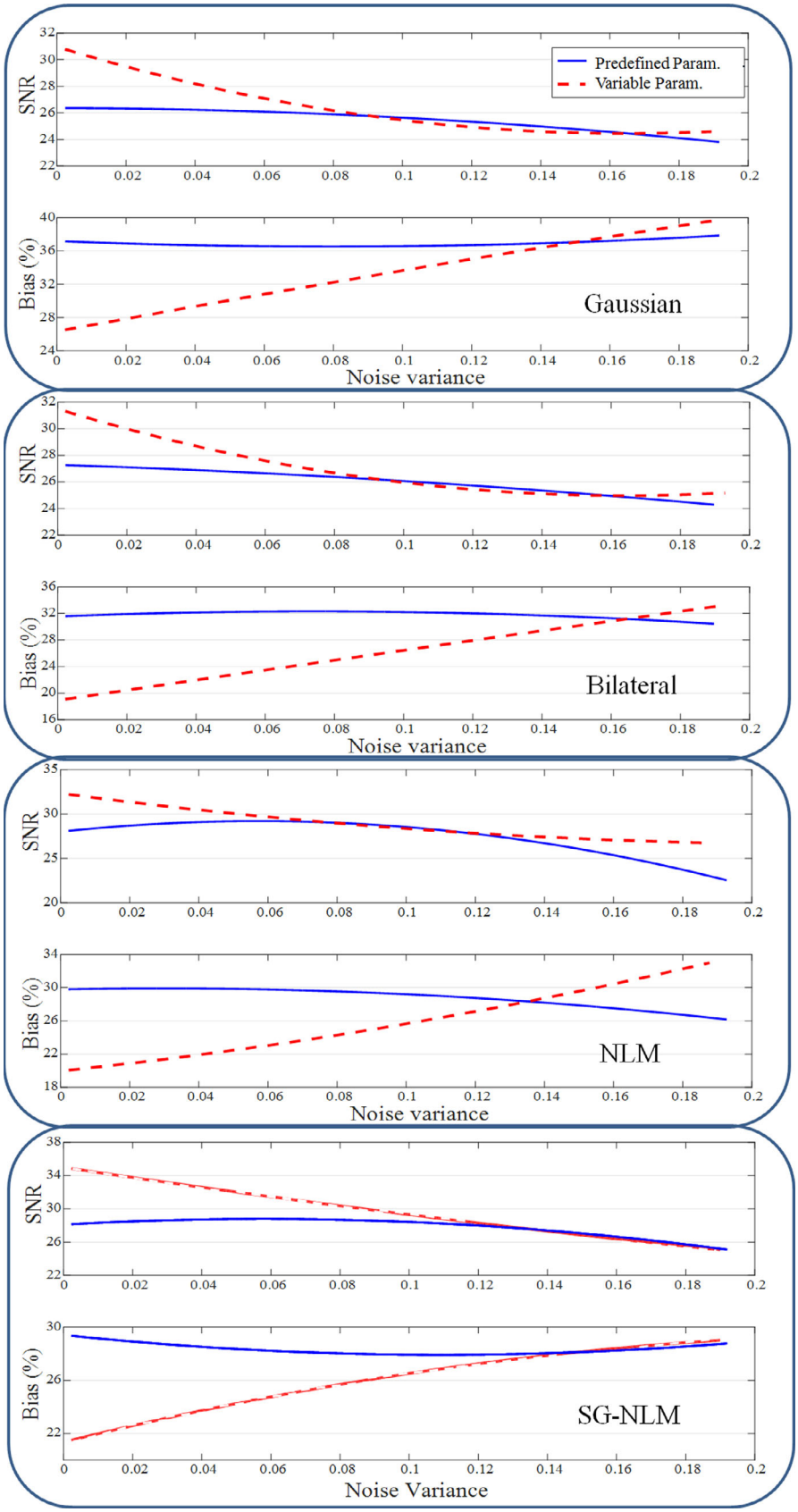

FIG. 7. Comparison of the quantification bias (%) and signal-to-noise ratio (SNR) measured on tumor number one (T1) in the thorax phantom after applying the Gaussian, bilateral, nonlocal mean (NLM), and spatially guided NLM denoising approaches using predefined parameters vs variable parameters suggested by the noise variance estimator. [Color figure can be viewed at wileyonlinelibrary.com]

attenuation correction are handled in the clinic, that pairs of PET images before and after undergoing denoising are used for visual inspection to take the advantage of the synergy between the human visual system and computer processing.

5. CONCLUSIONS

The spatially guided nonlocal mean filter was introduced as a variant of the conventional NLM filter which is capable of exploring the entire image to take advantage of redundant information present in the form of repeated patterns and prolonged edges as opposed to the conventional NLM filter where the nonlocal information extraction is confined to a predefined search window. A novel patch searching scheme was adopted using the clustered version of the input image as well as the information about prominent edges. Computer simulation and physical phantom experiments demonstrated the superior trade-off between signal preservation and noise elimination achieved by the SG-NLM filter compared to the conventional NLM filter as well as the Gaussian, bilateral, and BayesShrink Wavelet filters. More importantly, the clinical evaluation on 40 lesions revealed the reduced bias and increased signal-to-noise ratio when using the SG-NLM approach. The SG-NLM showed superior performance without adding extra burden to the computational complexity of the NLM filter, which makes it an attractive option for denoising of 3D images.

ACKNOWLEDGMENTS

This work was supported by the Swiss National Science Foundation under grant SNRF 320030_176052 and the Swiss Cancer Research Foundation under Grant KFS-3855-02-2016.

CONFLICT OF INTEREST

The authors declare that they have no conflict of interest.

[a)]Author to whom correspondence should be addressed. Electronic mail: habib.zaidi@hcuge.ch; Telephone: +41 22 372 7258; Fax: +41 22 372 7169.

REFERENCES

1. Zaidi H, Karakatsanis N. Towards enhanced PET quantification in clinical oncology. *Br J Radiol*. 2018;91:20170508.
2. Snyder DL, Miller MI, Thomas LJ, Politte DG. Noise and edge artifacts in maximum-likelihood reconstructions for emission tomography. *IEEE Trans Med Imaging*. 1987;6:228–238.
3. Nuyts J, Fessler JA. A penalized-likelihood image reconstruction method for emission tomography, compared to postsmoothed maximum-likelihood with matched spatial resolution. *IEEE Trans Med Imaging*. 2003;22:1042–1052.
4. Nuyts J, Baete K, Beque D, Dupont P. Comparison between MAP and postprocessed ML for image reconstruction in emission tomography when anatomical knowledge is available. *IEEE Trans Med Imaging*. 2005;24:667–675.
5. Qi J, Leahy RM. Iterative reconstruction techniques in emission computed tomography. *Phys Med Biol*. 2006;51:R541–R578.
6. Reader AJ, Zaidi H. Advances in PET image reconstruction. *PET Clinics*. 2007;2:173–190.
7. Turkheimer FE, Banati RB, Visvikis D, Aston JA, Gunn RN, Cunningham VJ. Modeling dynamic PET-SPECT studies in the wavelet domain. *J Cereb Blood Flow Metab*. 2000;20:879–893.
8. Shih Y-Y, Chen J-C, Liu R-S. Development of wavelet de-noising technique for PET images. *Comput Med Imaging Graph*. 2005;29:297–304.
9. Hofheinz F, Langner J, Beuthien-Baumann B, et al. Suitability of bilateral filtering for edge-preserving noise reduction in PET. *EJNMMI Res*. 2011;1:23.
10. Elad M. On the origin of the bilateral filter and ways to improve it. *EEE Trans Image Process*. 2002;11:1141–1151.
11. Pierazzo N, Facciolo G. Data adaptive dual domain denoising: a method to boost state of the art denoising algorithms. *Image Processing On Line*. 2017;7:93–114.
12. Arabi H, Zaidi H. Improvement of image quality in PET using post-reconstruction hybrid spatial-frequency domain filtering. *Phys Med Biol*. 2018;63:215010.
13. Vunckx K, Atre A, Baete K, et al. Evaluation of three MRI-based anatomical priors for quantitative PET brain imaging. *IEEE Trans Med Imaging*. 2012;31:599–612.
14. Chan C, Fulton R, Barnett R, Feng DD, Meikle S. Postreconstruction nonlocal means filtering of whole-body PET with an anatomical prior. *IEEE Trans Med Imaging*. 2014;33:636–650.
15. Buades A, Coll B, Morel J-M. A non-local algorithm for image denoising. IEEE Computer Society Conference on Computer Vision and Pattern Recognition (CVPR'05). 2005:60–65.
16. Dutta J, Leahy RM, Li Q. Non-local means denoising of dynamic PET images. *PLoS ONE*. 2013;8:e81390.
17. Wang G, Qi J. Penalized likelihood PET image reconstruction using patch-based edge-preserving regularization. *IEEE Trans Med Imaging*. 2012;31:2194–2204.
18. Xu Z, Bagci U, Seidel J, Thomasson D, Solomon J, Mollura DJ. Segmentation based denoising of PET images: An iterative approach via regional means and affinity propagation. Pa International Conference on Medical Image Computing and Computer-Assisted Intervention, MICCAI. Springer; 2014:698–705.
19. Xu Z, Gao M, Papadakis GZ, et al. Joint solution for PET image segmentation, denoising, and partial volume correction. *Med Image Anal*. 2018;46:229–243.
20. Arabi H, Zaidi H. Spatially-guided non-local mean filter for denoising of clinical whole-body PET images. 2018 IEEE Nuclear Science Symposium and Medical Imaging Conference Proceedings (NSS/MIC), pp 1–3.
21. Liu C, Freeman WT, Szeliski R, Kang SB. Noise estimation from a single image. IEEE Computer Society Conference on Computer Vision and Pattern Recognition. 2006:901–908.
22. Zitnick C, Jojic N, Kang SB. Consistent segmentation for optical flow estimation. Tenth IEEE International Conference on Computer Vision, ICCV; 2005:1308–1315.
23. Sobel I, Feldman G. "A 3x3 isotropic gradient operator for image processing," a talk at the Stanford Artificial Project. Pattern Classification and Scene Analysis; 1968:271–272.
24. Chang SG, Yu B, Vetterli M. Adaptive wavelet thresholding for image denoising and compression. *IEEE Trans Image Process*. 2000;9:1532–1546.
25. Paris S, Kornprobst P, Tumblin J, Durand F. Bilateral filtering: Theory and applications. Foundations and Trends® in Computer Graphics and Vision 4, 1–73; 2009.
26. Kim JH, Ahn IJ, Nam WH, Ra JB. An effective post-filtering framework for 3-D PET image denoising based on noise and sensitivity characteristics. *IEEE Trans Nucl Sci*. 2015;62:137–147.

SUPPORTING INFORMATION

Additional supporting information may be found online in the Supporting Information section at the end of the article.

Figure S1. Comparison of profiles drawn vertically on the three tumors in the digital thorax phantom before (OSEM) and after applying Gaussian, bilateral, BW, NLM and SG-NLM denoising approaches